



Journal of Geophysical Research: Solid Earth

RESEARCH ARTICLE

10.1002/2017JB014135

Kev Points:

- Joint inversion of and surface wave dispersions, receiver functions, and P velocity model were developed to reduce model ambiguity
- Flexible parameterization and addition of the V_{ρ} constraint were demonstrated to be crucial in improving model recovery and resolution
- Application to SE Tibet indicates only one region of prominent low velocities and high V_ρ/V_s ratio in mid-lower crust with possible melting

Correspondence to:

X. Song, xiao.d.song@gmail.com

Citation:

Li, J., Song, X., Zhu, L., & Deng, Y. (2017). Joint inversion of surface wave dispersions and receiver functions with *P* velocity constraints: Application to Southeastern Tibet. *Journal Geophysical Research*: *Solid Earth*, *122*, 7291–7310, https://doi.org/10.1002/2017JB014135

Received 24 FEB 2017 Accepted 29 AUG 2017 Accepted article online 4 SEP 2017 Published online 25 SEP 2017

Joint Inversion of Surface Wave Dispersions and Receiver Functions with *P* Velocity Constraints: Application to Southeastern Tibet

Jiangtao Li¹ , Xiaodong Song^{1,2} , Lupei Zhu³ , and Yangfan Deng^{1,4}

¹Department of Geology, University of Illinois at Urbana-Champaign, Urbana, IL, USA, ²School of Geodesy and Geomatics, Wuhan University, Wuhan, China, ³Department of Earth and Atmospheric Sciences, Saint Louis University, St. Louis, MO, USA, ⁴State Key Laboratory of Isotope Geochemistry, Guangzhou Institute of Geochemistry, Chinese Academy of Sciences, Guangzhou, China

Abstract We introduced a P velocity model into the traditional joint inversion of P receiver function (RF) and surface wave dispersions to reduce model ambiguity. The method was implemented using a global search-based algorithm and a flexible parameterization of a sedimentary layer and spline-based parameterization that can represent sharp discontinuities. We applied the method to a dense array in SE Tibet (longitude ~97.5°E to 107°E, latitude ~25.3°N). Extensive tests using synthetic and real data suggest that the method is suitable and robust for a variety of velocity structures and Moho discontinuities and can simultaneously provide the crustal V_0/V_s profile and better constrained Moho depth. The flexibility of the parameterization and the inclusion of the V_p constraint are crucial in the improved model recovery. Artifacts may be created without including the sedimentary layer. Even when it is less perfect, a reasonable V_n model is valuable in such a joint inversion. We showed that crustal multiples in RFs may bias the traditional H-k results when the crust structure is complex and should be avoided in a joint inversion before appropriate corrections can be made. The results from the joint inversion show two low-velocity zones (LVZs) reported previously and were identified as channels of crustal flow. A prominent isolated LVZ is observed in the mid-lower crust under the Xiaojiang fault area, which correlates with anomalously high V_p/V_s ratios, indicating possible partial melting. However, the other LVZ is imaged to be in the brittle shallow upper crust without very high V_D/V_S ratios, which is likely associated with crustal fault zones rather than partial melting. We observe clear low-velocity structures in the mantle beneath the two crustal LVZs, which also correlate with zones of low resistivity. The crust-mantle correlation may suggest influence of mantle processes on crustal deformation.

Plain Language Summary Nonunique in seismic inversion is a classical problem. The widely used inversion of surface wave dispersions or the joint inversion of dispersions and receiver functions suffers also the problem. In this study, we introduce *P* velocity model into the mix and adopted a flexible parameterization and inversion scheme, which we demonstrated to be robust and highly effective. We applied the method to a dense array in SE Tibet, which deforms strongly with active seismicity. The array was studied before, and two crustal flow channels were identified. The new imaging suggests that one low-velocity zone may indeed associated with partial melting with the additional constraint from the Poisson's ratio, but the other low-velocity zone is too shallow to be associated with partial melting. We also found significant mantle low-velocity zones, which may influence the crustal deformation of the region.

1. Introduction

Joint inversions of complimentary data sets have been widely used in seismic imaging to reduce the trade-off of model parameters and the ambiguity of inversion results. For instance, teleseismic P wave receiver functions (RFs) (Langston, 1979) are sensitive to velocity contrast and depth-velocity product instead of absolute velocity alone, while surface wave dispersions are sensitive to vertical shear-velocity average but do not resolve discontinuities (Ammon et al., 1990; Shapiro & Ritzwoller, 2002). Thus, the two data sets are combined to address the trade-off between the depth of an interface (especially the Moho) and the average velocity above the interface (e.g., Julià et al., 2000; Ozalaybey et al., 1997), which has been commonly used (e.g., Bao et al., 2015a; Deng et al., 2015; Shen et al., 2013; Sun et al., 2014; Xu et al., 2013). However, important ambiguity remains. In the P receiver function, the Moho P-to-P converted phase (P) is generally the strongest. The result of joint inversion (especially the Moho depth) is greatly influenced by the V_P/V_S ratio in the crust,

©2017. American Geophysical Union. All Rights Reserved.

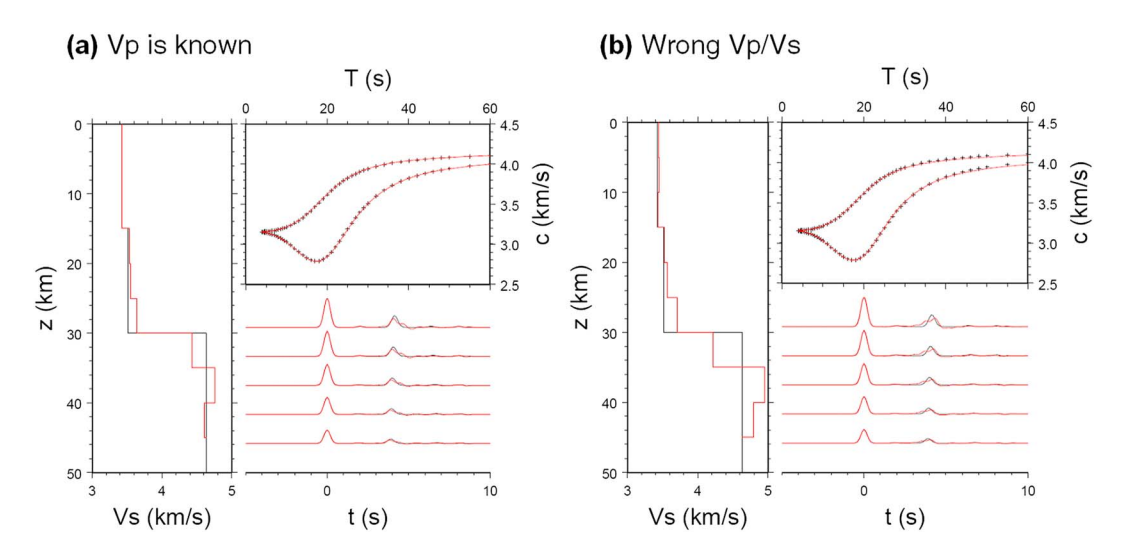


Figure 1. Synthetic tests on joint inversion of receiver functions and surface wave dispersions, with and without prior knowledge of V_p structure. (a) V_p is set to the true values. Inverted V_s (red) matches the input model (black) relatively well. (b) V_D/V_S ratio is set to 1.7 (compared to the average 1.8 of the input model). Inverted V_S does not match the input as well as in Figure 1a, while the fits to dispersions (top right) and receiver functions (bottom right) are similar.

which is often unconstrained and normally set to the global average (1.75). Multiple converted phases (the well known H-k method) can help resolving the ambiguity (Zhu & Kanamori, 2000). However, they are usually more difficult to identify and in places where the crust is complex, the H-k method can also be strongly biased because the multiples are more sensitive to crustal complexity (see below).

Sensitivity tests (Figures 1 and 2) suggest that adding independently constrained P information will help the joint inversion of receiver function and surface wave dispersion to find the right S model when the V_D/V_S ratio is not known. The tests are done based on the method by Xu et al. (2013), using a simple model with either fixed crustal V_p or fixed V_p/V_s . The synthetic case shown in Figure 1 assumes that P velocity profile as a function of depth in the crust is known. The information can come from P wave tomography or a wide-angle

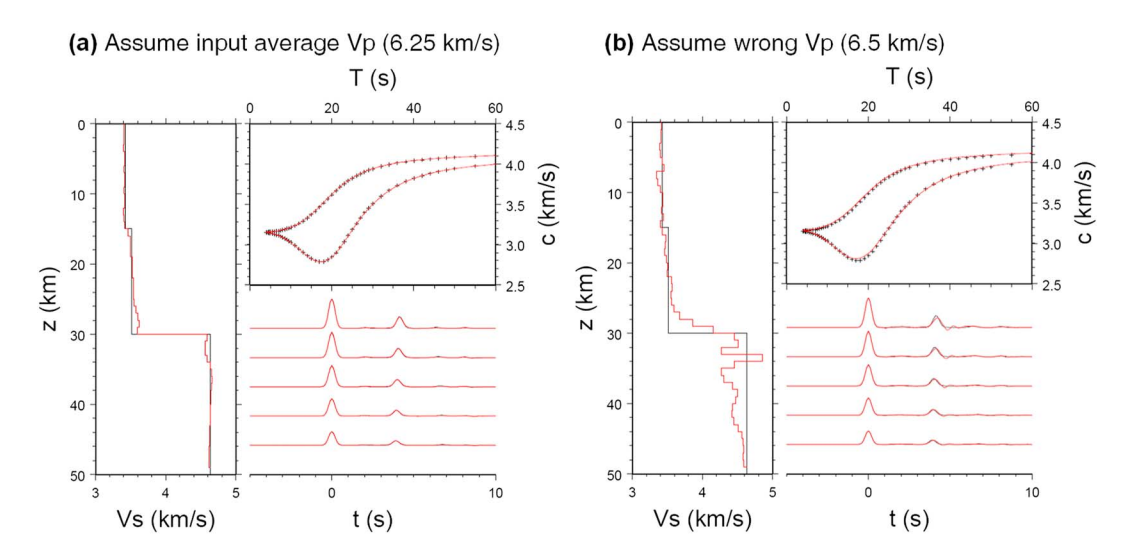


Figure 2. Same as Figure 1 but with and without prior knowledge of average V_D in the crust (e.g., from Pn station delay). (a) Correct average crustal V_D (6.25 km/s) is assumed, which would yield the correct input Moho depth (30 km) and produce the correct input Pn delay time. (b) Average crustal V_p is assumed to be a wrong value of 6.5 km/s, which would put the Moho at 33.3 km in order to match the correct Pn delay time in Figure 2a. The inverted S structure recovered is considerably poorer than in Figure 2a and has a Moho (at 30 km or slightly less) incompatible with the Moho (33.3 km) from the Pn delay time.



Table 1 Sensitivities of Crustal Parameters to Different Data Types ^a				
	V_p	V_s	V_p/V_s	Moho
SW dispersion		Х		
Receiver function (Ps conversion)			X	Χ
P velocity model	Χ			
Pn station delay	Χ			Х
3				

^aCheckmark indicates primary sensitivity of parameter to data type.

refraction survey. The synthetic test in Figure 2 assumes that the average *P* velocity beneath the station is known, for example, from the station-delay time term in a *Pn* traveltime tomography (e.g., Hearn, 1996; Liang et al., 2004; Liang & Song, 2006). In either case, the synthetic tests suggest that the joint inversion including the *P* information achieves considerably better recovery of the input S model (Figures 1 and 2). Table 1 summarizes the primary sensitivity of each data set if we rely on the *Ps* phase. Adding independent *P* information provides an important constraint for the *S* velocity structure in a joint inversion with surface-wave dispersion and receiver function.

The Tibetan Plateau, the largest and highest plateau in the world, is resulted from the Cenozoic Indian-Eurasian collision (Molnar & Tapponnier, 1975; Yin & Harrison, 2000). Despite decades of studies, the mechanism of its uplift and growth is still in debate. Three end-member models have been proposed, including rigid block extrusion (Molnar & Tapponnier, 1975; Tapponnier et al., 2001), continuous deformation (England & Houseman, 1986; Zhang et al., 2004), and mid-lower crustal flow (Clark & Royden, 2000; Royden et al., 1997, 2008). As a margin of the Tibetan Plateau with strong deformation and active seismicity, the SE Tibet has been an ideal location to test different hypotheses.

Several lines of evidence have suggested that much of the mid-lower crust beneath the Tibetan Plateau and its eastern surroundings may be partially molten, including surface wave tomography (Bao et al., 2015b; Chen et al., 2016; Li et al., 2014; Sun et al., 2010; Yang et al., 2012; Yao et al., 2008), joint inversion of RFs and dispersions (Bao et al., 2015a; Li et al., 2016; Sun et al., 2014; Xu et al., 2013; Zheng et al., 2016), seismic attenuation (Hearn et al., 2008; Zhao et al., 2013), and magnetotelluric studies (Bai et al., 2010; Dong et al., 2016; Le Pape et al., 2012). However, it is still debated whether the low-velocity, low-resistivity layer is present extensively or limited to certain localities or channels, what its properties are, how it deforms, and what role it has played in plateau's evolution (Agius & Lebedev, 2014).

In this study, we present a scheme for joint inversion of surface-wave dispersion and receiver function with constraint of *P* velocity-depth profile. We tested the method by applying to a dense array of seismic stations in SE Tibet (Figure 3) from ChinArray-Himalaya (2011), which was used previously by Sun et al. (2014)

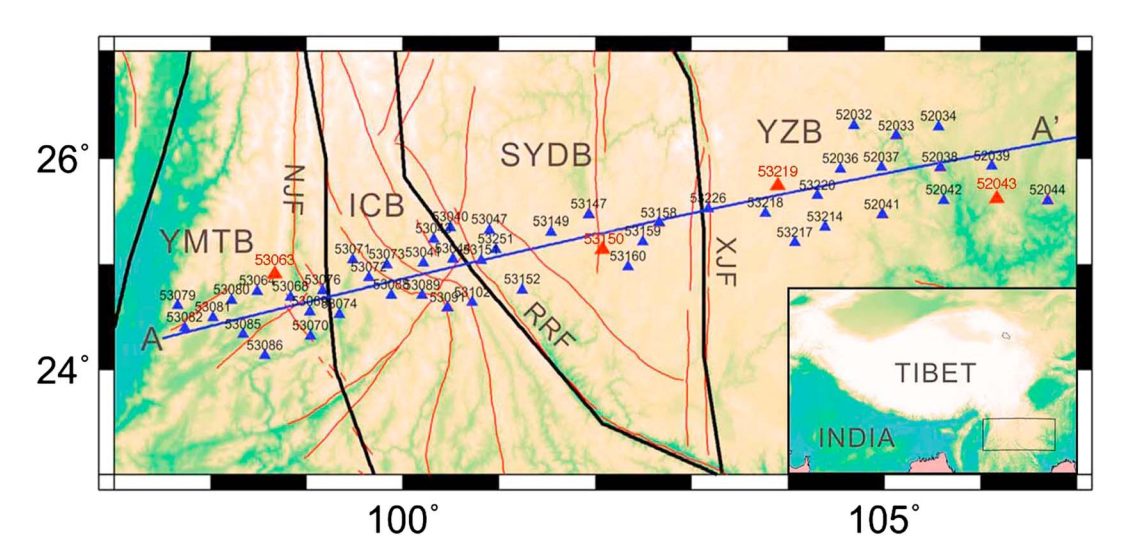


Figure 3. Distribution of seismic stations (triangles) with surface topography and geological elements. Inset shows the location of the study region. The red triangles are the four example stations for demonstrations. The red lines represent faults, and the black lines are the boundaries between major blocks. The blue line AA' is the profile shown in the following figures. (NJF, Nujiang fault; RRF, Red River fault; XJF, Xiaojiang fault; YMTB, Yunnan-Myanmar-Thailand block; ICB, Indo-China block; SYDB, Sichuan-Yunnan diamond block; YZB, Yangtze block). Figure adapted from Sun et al. (2014).



(hereafter referred to as SUN14) for the joint inversion of dispersion and receiver function. The array cuts across several major crustal blocks of the region, including the Yunnan-Myanmar-Thailand block (YMTB), the Indo-China block (ICB), the Sichuan-Yunnan Diamond block (SYDB), and the Yangtze block (YZB), which are separated by the Nujiang fault (NJF), the Red River fault (RRF), and the Xiaojiang fault (XJF) from west to east (Figure 3). SUN14 found two significant low-velocity zones (LVZs) in the middle and mid-lower crust, respectively, which were interpreted as isolated channels of crustal flow at different depths beneath SE Tibet. The two channels were further identified throughout SE Tibet by Bao et al. (2015a), also using joint inversions of surface-wave dispersions and RFs. Separately, several *P* wave tomography studies have been done in this region (Huang et al., 2009, 2015, 2002; Lei et al., 2009; Wang et al., 2003; Wei, Sun, & Shi, 2010; Xu & Song, 2010), providing independent constraint on crustal *P* velocities. We will compare our new inversion with the previous results. Below we give details of the methodology and the new joint inversion results, extensive tests of the methodology using synthetic and real data, comparison of the results using different data sets or assumptions, implications of the joint inversion results, and issues of using crustal multiples when the crustal structure is complex.

2. Development of Method for Joint Inversion of RFs and Dispersions With *P* Velocity Constraints

Our joint inversion of surface-wave dispersions and RFs with P velocity constraints (JP) is modified from the implementation of Xu et al. (2013) for the joint inversion of surface wave dispersions and RFs (SD + RF), which designed an elaborate joint inversion scheme using the Neighborhood Algorithm (NA) (Sambridge, 1999) to determine the lithospheric S velocity structure. They used two sets of stretchable splines in the inversion to obtain smooth velocity profiles, separated by a specifically defined Moho (the connecting node of the crustal and mantle splines, the depth of which is allowed to change as a search parameter), and implemented the message passing interface (MPI) for parallel processing, which greatly reduced the computation time. However, without independent P wave information, the crustal V_p/V_s ratio is fixed to 1.75 in their inversions (Xu et al., 2013). Our modification in this study includes incorporating P velocity model in the joint inversion, unfixing V_p/V_s ratios in the crust, and changing parameterization of the crust (adding a sedimentary layer on top and changing node spacing of the crustal spline function).

The JP is done for one station at a time. For each station, the inputs include the crustal V_p profile as given, one stacked RF, and group and phase velocity dispersions. The V_p depth profile is fixed to the input model during the inversion as known. We used one stacked RF at a reference ray parameter (normally 0.06 s/km), rather than several RFs at different ray parameters, because we found that the difference is small. On the other hand, the stacking into one RF can enhance further the coherency of the Ps arrival. The forward calculation subroutines for dispersion curves and RFs are adopted from the Computer Programs in Seismology (Herrmann, 2013). We also use the fast global searching method NA (Sambridge, 1999), which provides great flexibility on parameterization. The global search is to minimize the misfit of the RF and dispersions with model damping and smoothing. The objective function is constructed as

$$\min \Big(w_1 \big\| D_{\text{obs}} - D_{\text{pred}} \big\|_{\text{rf}} + w_2 \big\| D_{\text{obs}} - D_{\text{pred}} \big\|_{\text{disp}} + \lambda \|m - m_0\| + \varphi \|Lm\| \Big). \tag{1}$$

The D indicates data (observed or predicted; RF or dispersion); m is model parameter (S velocity or interface depth) and m_0 is the reference model (see below); parameters w_1 and w_2 are the relative weighting factors for RF and dispersion misfit, respectively; L is the Laplacian smoothing operator (which is just the second derivative operator for the one-dimensional case); λ is the damping parameter; and φ is the smoothing parameter. The last two terms determine the influence of the initial model and the smoothness of the model, respectively. Before the JP, we first perform an inversion using one cubic spline with a uniform node spacing for the crust and the mantle (a total of 15 nodes from surface to depth of 150 km) and using dispersion data only to obtain an S velocity profile at each station as the initial model for the JP, which can help the search to converge faster (Xu et al., 2013).

In the model parameterization, we introduce a separate sedimentary layer at the surface, which has a great influence on the waveform of the RF, particularly the beginning portion of the RF (direct *P* energy). We use a

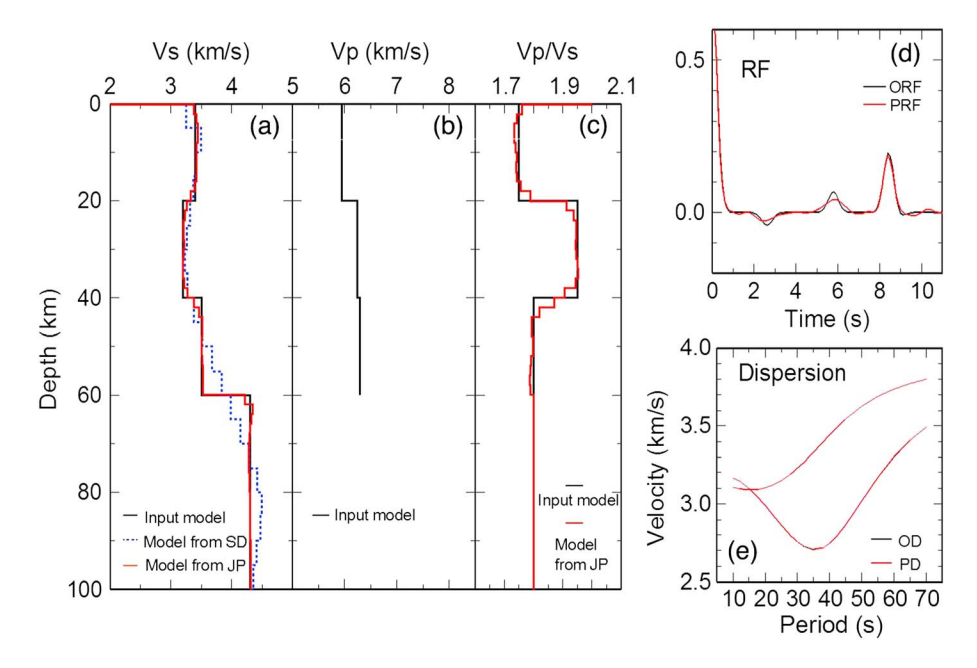


Figure 4. Synthetic test of the joint inversion of RF, dispersions, and V_p model (JP). The input velocity model has three layers in the crust and one layer in the mantle. The input model or input data, the result from surface wave dispersion (SD) inversion alone, and the results for the JP are shown in black, blue dashed, and red lines, respectively. (a) Input V_s model and inversion results. (b) Input V_p model. (c) Input V_p/V_s model and inversion result from JP. (d) The observed RF (ORF) and the predicated RF (PRF) from the best fitting model of the JP. (e) The observed Rayleigh wave group and phase dispersion (OD) curves and the predicated dispersion (PD) curves from the best fit ting model of the JP.

linear gradient in S velocity for the sedimentary layer but allowed the thickness and top and bottom velocities to vary. We fix the V_p/V_s ratio for the sedimentary layer at 2.0 (Shen et al., 2013) as it has some trade-off with the layer thickness and fix the V_p/V_s for the mantle at the global average of 1.8. The splines of V_s are interpolated into layers with an interval of 0.1, 2, and 5 km in the sedimentary layer, crust, and uppermost mantle (30 km below the Moho), and deeper mantle, respectively. The layered crustal V_p/V_s is determined by the V_s from inversion and the interpolated V_p at the same depth (or extrapolated if deeper than the given crustal V_p profile). The density is calculated by the Nafe and Drake (1963) relationship. The crust and the mantle are parameterized as cubic splines, with fixed numbers of nodes of 12 and 9, respectively. The bottom node of the crustal spline has the same value as the top node of the mantle spline so that the model is always continuous below the sedimentary layer (including the Moho). We allow the depth of the connecting node between the crust and mantle to vary, which is defined as the Moho. The depth of the last (bottom) node in the mantle is fixed at 150 km. Thus, the spacing between the spline nodes varies as the Moho depth changes. We used a stretching spline for the mantle part so that the node spacing is smaller closer to the Moho to improve the resolution near the Moho, which is extremely effective in representing the Moho whether it is gradual or sharp (Xu et al., 2013). However, we set uniform node spacing for the crust, unlike in Xu et al. (2013), which has a setup similar to the mantle with smaller spacing near the surface to represent the strong gradient. Since a sedimentary layer at the surface is already defined separately, such a stretching spline for the crust is no longer needed. The uniform spline in the crust increases the resolution in the middle and lower crust.

Thus, the search parameters are three sedimentary layer parameters (layer thickness and S velocities at the top and bottom), S velocities at the 20 spline nodes for the crust and mantle (with one connecting node at the bottom of the sedimentary layer and another connecting node at the Moho), and the Moho depth. The model constraint m_0 consists of two parts: one from the initial spline based on inversion of dispersions only and the other from Bao et al. (2015b) for depths below 95 km, where the sensitivity of our dispersion data decreases. The implementation uses parallel programming with MPI calls, which greatly speeds up the model search with parallel machines. For each station, we generate 200 random models to start with,



and then iterate 2000 times to obtain the final model. Consequently, the total models generated for each point is 200,200. The best fitting model is our final model.

Figure 4 shows a synthetic test to demonstrate the robustness of our method. The input model has three layers in the crust, which includes a low-velocity and high- V_D/V_S zone in the middle crust over a half-space of constant velocity in the mantle. The JP recovers well the input V_s and V_p/V_s model, including the discontinuity depths as well as the V_s and V_p/V_s values. The predicted RF and dispersion curves for the inverted final model agree well with the input ("observed") data. To demonstrate the effectiveness of our method on different velocity structures, we performed eight more synthetic tests with different velocity features (e.g., no LVZ, lower crust high velocity, higher-mantle velocity, different sedimentary layer thickness, or Moho depth), which suggest that our joint inversion method can work robustly for various velocity structures (Figure 5).

3. Application to Stations in SE Tibet

3.1. Data

The data used in this study include three types: P wave RFs (of the Ps converted phase), dispersion curves of surface wave group and phase velocities, and crustal P velocity model (Figures 6a-6d; note that Figure 6d shows the inversion result of dispersion data set for direct comparison with other inversions). These data were assembled from seismic stations roughly along a linear array in SE Tibet (Figure 3).

The RFs were from SUN14, which were calculated from teleseismic P waveforms recorded by 51 temporary broadband stations (Figure 3) between August 2011 and August 2012. The stations are part of the ChinArray program (Ding & Wu, 2013) deployed by the China Earthquake Administration (CEA) and the Nanjing University since September 2010, with an average station interval of ~35 km. We stacked all the RFs with clear Ps phase of each station into one RF after moveout correction (Yuan et al., 1997) at a reference slowness of 6.4 s/deg using the IASP91 model (Kennett & Engdahl, 1991). The Gaussian width used was 2.5 (Langston, 1979). We cut the RFs within 15 s to limit the crustal multiples because they are more complicated than the Ps phase, which may bias the inversion results (see discussion in section 4.3).

The dispersion data were from our recent surface wave tomography of mainland China (Bao et al., 2015b) using both ambient noise and earthquake data, which has a resolution of 1° in the SE Tibet. It included 864 CEA permanent stations from 2008 to 2011, 401 temporary PASCCAL stations, and 51 permanent stations from the Incorporated Research Institutions for Seismology Data Management Center. More than 700,000 dispersion curves were measured to generate group and phase velocity maps at periods of 10-140 s and 10-70 s, respectively. In this study, we extracted group and phase velocity dispersion curves at each of our stations from the dispersion maps of 10-70 s, which are better constrained with both the ambient noise and earthquake data.

We extracted the crustal P velocity-depth profile for each station of the array from the 3-D tomographic model by Xu and Song (2010). The study included the Chinese national and provincial earthquake bulletins as well as some handpicked arrivals from 1981 to 2003, with 12,509 events and 250 stations, and forming a total of 97,099 raw traveltime picks. They used first-arriving Pq to sample the upper-to-mid crust, secondary Pq (after the Pq-Pn crossover distance) to sample the mid-to-lower crust, and Pn phase to sample the uppermost mantle and designed an iterative scheme to jointly invert for crustal P velocity, Pn velocity, and the Moho depth. The resolution of crustal P velocity can reach 1° in most of the SE Tibet.

Because of active seismicity and dense distribution of seismic stations, several P wave tomographic studies have been conducted in SE Tibet. We have compared them to examine the consistency, particularly along the profile of our station array. Most of them (Huang et al., 2002, 2009, 2015; Lei et al., 2009; Wang et al., 2003; Wei et al., 2010) used first P (Pq and Pn) arrivals from China Seismic Network bulletins of local earthquakes, while Wei et al. (2010) also used mantle P waves to image the upper mantle. Lei et al. (2009) and Huang et al. (2015) also included relative traveltime residuals of teleseismic events, since their studies were more focused on the deeper part. However, none of the studies have included the secondary Pg phases. The method used in all of these studies was based on Zhao et al. (1992) or later versions, which used 3-D ray tracing that can work for models with complex-shaped discontinuities (e.g., Conrad and Moho). The Moho discontinuity in all the studies was assumed a priori from other studies. Most of the models are generally consistent at similar depths.

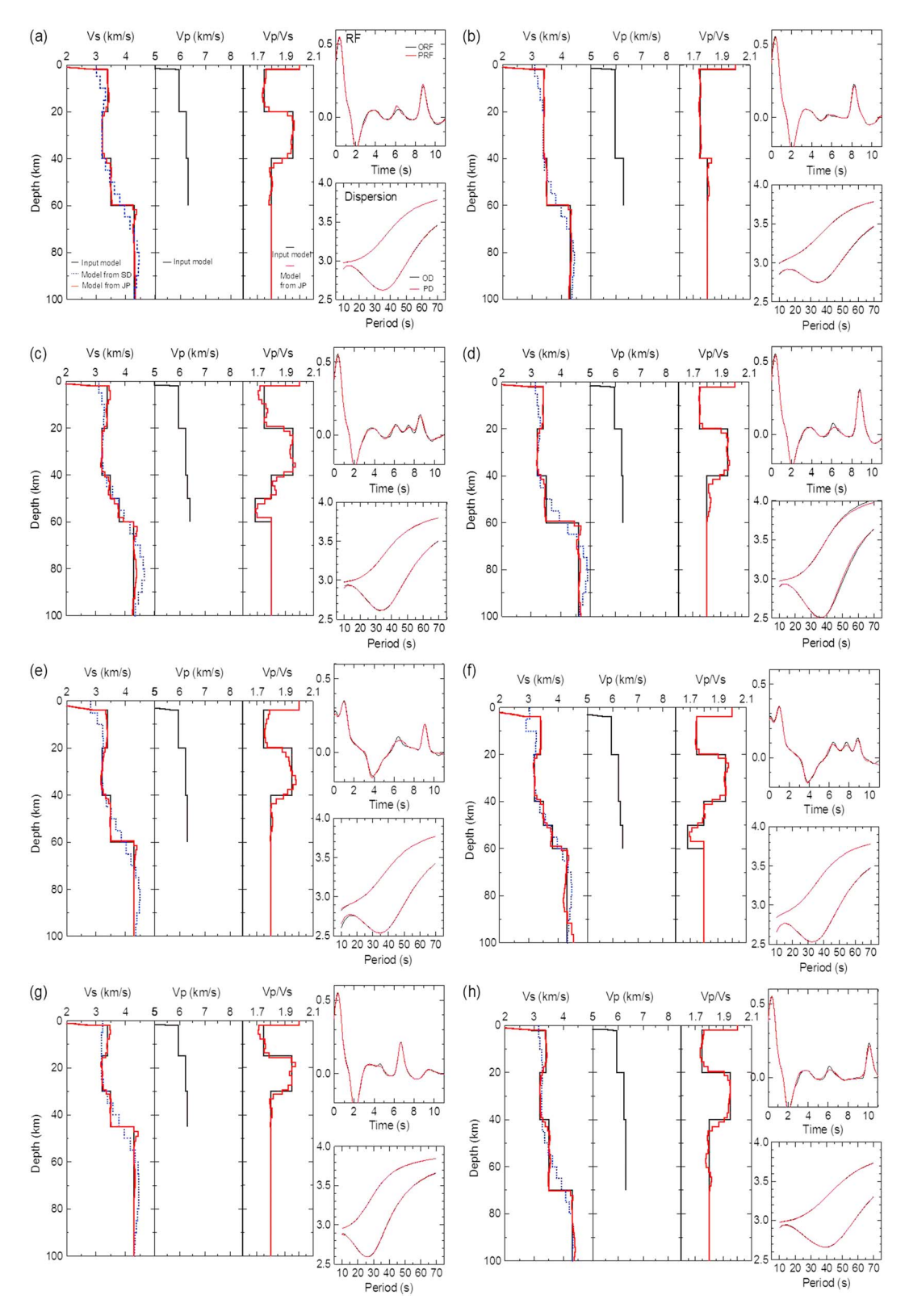


Figure 5. Synthetic tests of the JP for various synthetic cases. (a) The input model has a 2 km thick sedimentary layer compared with Figure 4. (b) The input model does not have LVZ compared with Figure 5a. (c) The input model has a high-velocity zone (HVZ) compared with Figure 5a. (d) The input model has a higher velocity in the mantle compared with Figure 5a. (e) The input model has a 4 km sedimentary layer compared with Figure 5a. (f) The input model has a high-velocity layer in the lower crust compared with Figure 5e. (g) The input model has a Moho depth of 45 km compared with Figure 5a. (h) The input model has a Moho depth of 70 km compared with Figure 5a.

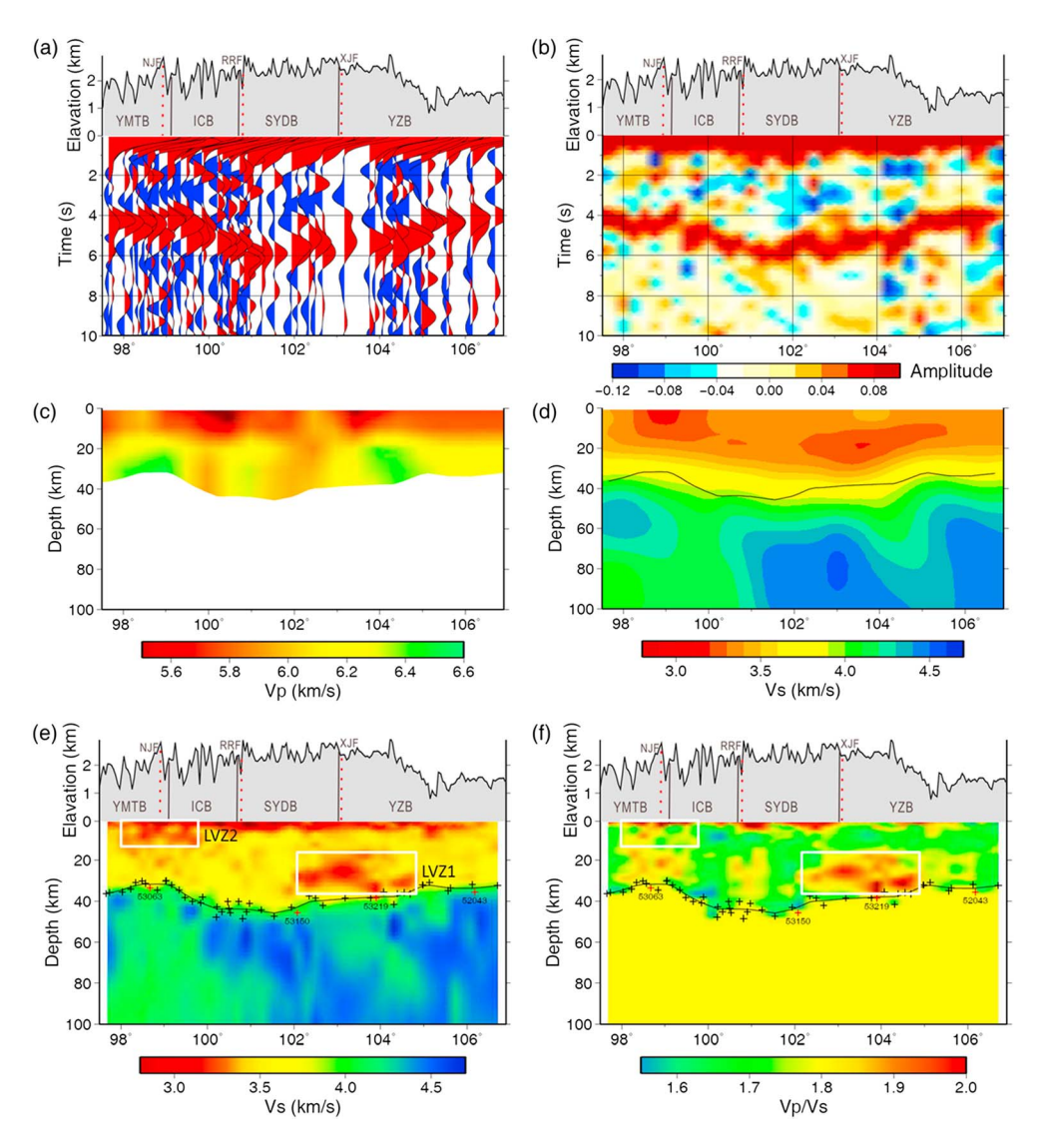


Figure 6. The three data sets used in (a–d) the JP and (e and f) the final JP results. Stacked RF profile from Sun et al. (2014) in waveform and amplitude, respectively (Figures 6a and 6b). V_p profile from Xu and Song (2010) (cut at the smoothed Moho depth from the JP) (Figure 6c). V_s profile from Rayleigh wave group and phase velocity dispersions by Bao et al. (2015b) (Figure 6d). Used in the JP are the dispersion curves at each station. The final V_s profile from the JP (Figure 6e). The V_p/V_s profile from the JP (Figure 6f). Topography and geological elements are shown at the top. The black crosses mark the Moho, and the red crosses are the four example stations. The black line show the smoothed (spline fit) Moho. The white boxes mark the two LVZs in the crust discussed in the text.

We chose the model by Xu and Song (2010) (which is readily available) for our joint inversion because of several reasons. First, the model included secondary Pg arrivals, which are clearly observed and provide an additional constraint on the mid-lower crust. Second, it included high-quality handpicked arrivals in the period from 1981 to 2003 besides bulletin picks. Third, it has one of the largest data set of local earthquakes in the study area compared with the cited studies. Fourth, the crust, Moho, and mantle are parameterized separately so that the sharp crust and mantle boundary (Moho) do not need to be artificially interpolated like in almost all tomographic studies. The parameterization allows us to use the whole P model throughout the crust that is constrained by the original traveltime data. This is particularly useful in our joint inversion as the Moho originally from the P traveltime inversion may not agree exactly with the final result of the joint inversion. The fidelity of the P model for the whole crust allows us to extrapolate with confidence to a greater depth when the joint inversion requires it, simply because the crust was originally parameterized as such (see

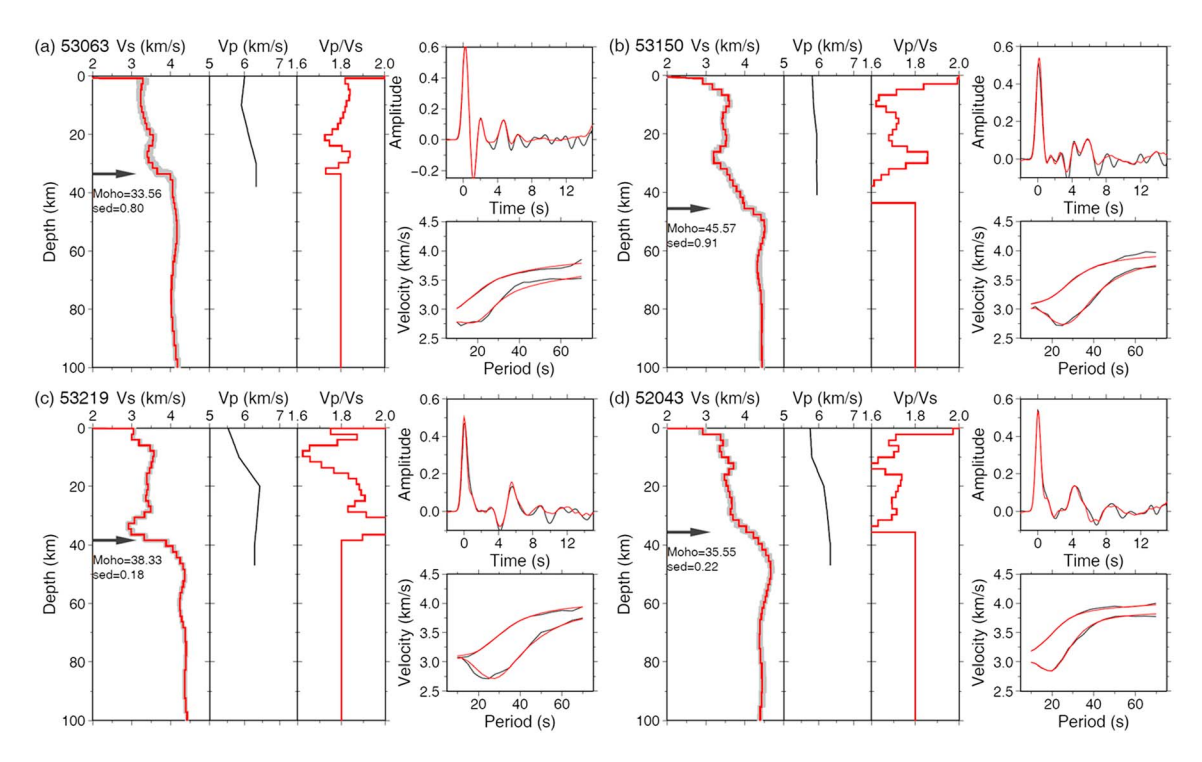


Figure 7. Four examples of the JP using real data. The panels for each station are the best fitting V_s model (red) with the 10,000 best models (grey) to show the uncertainty, the input V_p model from Xu and Song (2010), the V_p/V_s from the JP, the observed (black) and predicted (red) RF, and group and phase dispersion curves, respectively. The four stations have distinctly different velocity structures: (a) 53063 with a shallow LVZ to ~12 km and a small lower-crust LVZ, (b) 53150 with a distinct high-velocity, low- V_p/V_s layer in lower crust and a small midcrust LVZ, (c) 53219 with clear mid-lower crust LVZ and anomalously high V_p/V_s in lower crust, and (d) 52043 with a gradual Moho.

details in Xu & Song, 2010). Finally, the V_p perturbations in almost all the models above are consistent with Xu and Song (2010) along the station array in the crust.

3.2. Examples From Selected Stations

To demonstrate that our method works for different types of structures, we selected four representative stations (from the west to the east) of the JP results as displayed in Figure 7, the locations of which are shown in Figures 3 and 6e and 6f. The four stations are representative of the diverse velocity features in the study region. Station 53063 has a shallow LVZ down to ~12 km and also a small LVZ in lower crust. Station 53150 has a distinct high-velocity, low- V_p/V_s layer in lower crust, which corresponds to the large positive amplitude before the Ps phase, and also a small midcrust LVZ. Station 53219 has a broad LVZ from middle to lower crust, especially an anomalously low- V_s and high- V_p/V_s layer in lower crust. Station 52043 has a gradual Moho transition, which is indicated by the wide Ps phase in the RF. These models show diverse structures, which the method can all find to fit the data well. The RFs and dispersions were recovered very well by the final models.

3.3. Joint Inversion Results Along the Station Array

The final results of V_s and V_p/V_s profile from the JP are shown in Figures 6e and 6f. Figure 6e shows that there are two distinct LVZs besides the surface sedimentary layer, one in the mid-lower crust at about 102°E to 104.8°E (hereafter called LVZ1) and the other in the shallow upper crust (down to depth of about 14 km) at about 98°E to 99.8°E (hereafter called LVZ2). The Moho depth increases from ~35 km under YMTB to the largest depth of the profile of ~48 km under ICB and southern SYTB, and shallows gradually to ~40 km below the large LVZ under northern SYTB and southern YZB, and decreases further to less than 35 km under northern YZB. In the mantle, there are also two large LVZs, the locations of which seem to correlate with the two crustal LVZs. It is noticeable that the Moho seems to be shallower in these two regions compared to their surroundings of similar topography, which together might suggest additional buoyancy of mantle upwelling. The V_p/V_s profile (Figure 6f) displays a region with some very high V_p/V_s ratios (larger than 1.9), which is

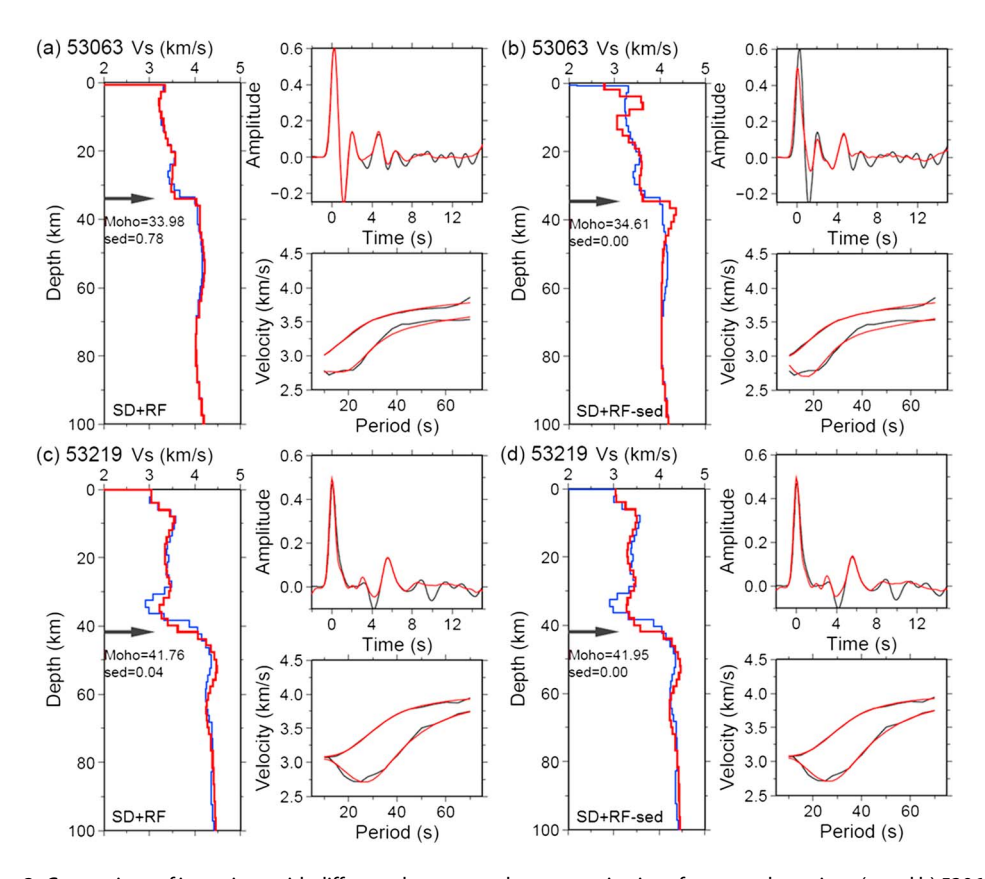


Figure 8. Comparison of inversions with different data sets and parameterizations for example stations (a and b) 53063 and (c and d) 53219, respectively. The inversion results and synthetics are in red, and the observed RFs and dispersion curves are in black. The examples show joint inversions with surface-wave dispersions and receiver functions (SD + RF) only (by fixing V_p/V_s at 1.75) that include (Figures 8a and 8c) or do not include (Figures 8b and 8d) a sedimentary layer in the parameterization. The inversion results are to be compared with those from the JP (blue) shown in Figures 7a and 7c, respectively.

almost at the same location of LVZ1, suggesting possible partial melt. However, at the location of LVZ2, there are only a few spots with slightly high V_p/V_s ratios. We will compare the results with previous study by SUN14 along the same profile below.

4. Discussion

4.1. Sensitivity Studies

To explore sensitivity and robustness of model parameters, we compare results using our new joint inversion scheme and previous methods. We compare inversions with and without a V_p constraint, a top sedimentary layer, or a V_p/V_s constraint.

4.1.1. Examples of Joint Inversions With/Without V_p Constraint and/or a Sedimentary Layer

Figure 8 shows results without a V_p model (i.e., by fixing V_p/V_s value to 1.75) and/or a sedimentary layer for two stations (53063 and 53219). The results from the JP (which includes V_p profile and sedimentary layer) for the two stations have been shown in Figures 7a and 7c, respectively.

Station 53063 was selected as an example to show the effect of the sedimentary layer (Figures 8a and 8b). The result from the joint inversion of RF and surface wave dispersion only without the V_p model is very similar to that of the joint inversion including the V_p model (Figure 8a). The results have a similar sedimentary thickness of ~0.8 km and a Moho depth (differing less than 0.5 km). This is not surprising as the averaged V_p/V_s ratio for the joint inversion with the V_p model is about 1.805, close to the default value of 1.75 used in the joint inversion without the V_p model. However, the joint inversion of RF and dispersions without a sedimentary layer (Figure 8b) show very different velocity structure in upper crust, which has a high-velocity layer followed by a prominent LVZ in order to fit the beginning part of RF. Because of the trade-off between difference depths, the structure at greater depths also shows some difference between the two inversions as well. In

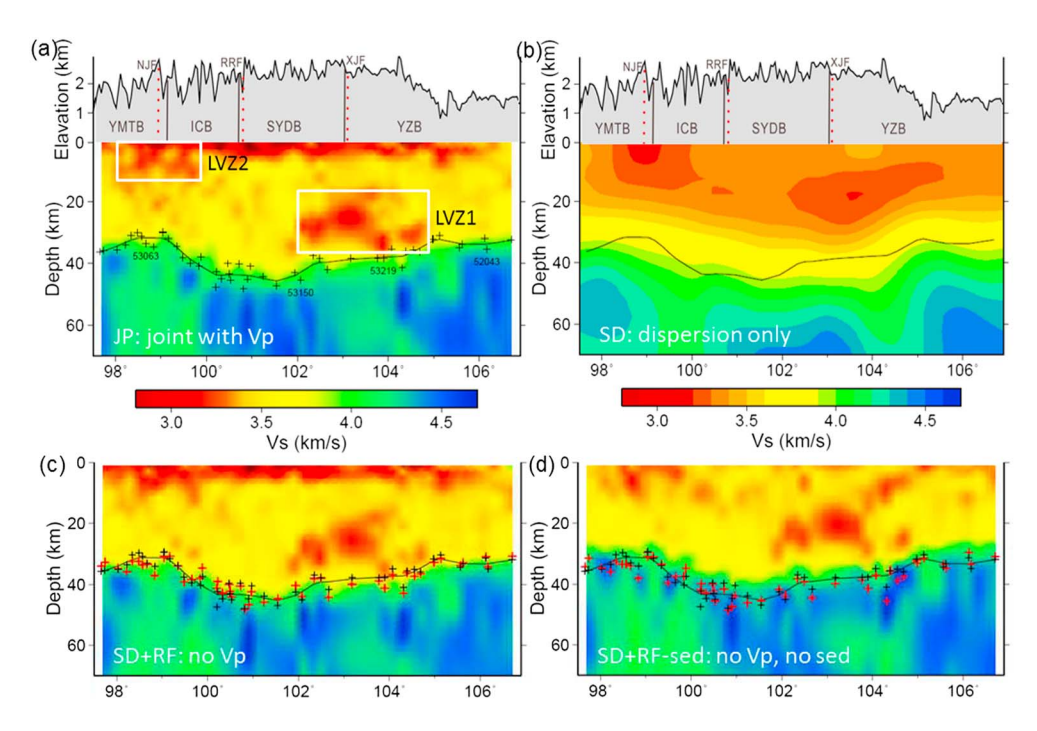


Figure 9. Comparison of the S velocity profiles from different inversions. (a) V_S profile from the JP (enlarged view of Figure 6e). (b) V_S profile from surface wave dispersions (SD) only (Bao et al., 2015b). (c) V_S profile from joint inversions of dispersions and RFs (SD + RF) only. (d) V_S profile from joint inversions of dispersions and RFs without a sedimentary layer (SD + RF-sed). Topography and geological elements are shown at the top. The black crosses in Figures 9a, 9c, and 9d mark the Moho from the JP, and the black line in all the plots shows the same smoothed Moho as in Figure 6 from the JP. The red crosses in Figures 9c and 9d mark the Moho from the corresponding inversion to be compared with the Moho from the JP (black crosses).

fact, even with such prominent features, the RF waveforms do not fit well. On the other hand, by having a thin sedimentary layer of ~0.8 km, the amplitude and shape of the beginning part of the RF can be recovered quite well. The example demonstrates the importance of incorporating properly the sedimentary layer at the surface, even when the layer is thin. Without including such a layer the inversion may result in artifacts.

Station 53219 was selected as an example to show the effect of incorporating a V_p model constraint (without fixing the V_p/V_s ratio) (Figures 8c and 8d). The example does not need a sedimentary layer to fit the P waveform of the RF. The joint inversions with V_p model (Figure 7c) can fit the large negative amplitude before the Ps phase in the RF much better, and thus revealing the low- V_s in lower crust more clearly, compared with using fixed V_p/V_s (Figures 8c and 8d). In this case, the average crust V_p/V_s ratio is about 1.853, much greater than the default value of 1.75. The high average crustal V_p/V_s also causes the Moho to be ~3.5 km shallower in the joint inversion with V_p .

4.1.2. Comparison of Different Inversions

Figure 9 compares results from different inversions, which shows consistent features as well as significant differences when different data sets or inversion assumptions are used. The inversions include the joint inversions with V_p and other data sets (JP) (Figure 9a), with dispersion only (SD) (Figure 9b), with RF and dispersion only (SD + RF) (Figure 9c), and with RF and dispersion only but without including a sedimentary layer (SD + RF-sed) (Figure 9d). All the images show the two low-velocity zones (LVZ1 and LVZ2) and the similar trend of the Moho undulations.

However, the detailed structures vary significantly, including shapes and depths of the LVZs and the depths of the Moho. By comparing SD + RF and SD + RF-sed, it is clear that the sedimentary layer can make a big difference on the crustal structure. Without a sedimentary layer (Figure 9d), some artificial LVZs in the upper crust are created to fit the beginning part of RFs. The LVZ1 structure is deeper and closer to the Moho in both JP and SD + RF than in SD + RF-sed. An artificial high-velocity layer above the Moho can also be seen in SD + RF-sed. The LVZ1 in SD is not only broader (due to the averaging effect of the dispersion data) but also much shallower than in JP and SD + RF. The LVZ2 in SD is broader but extends deeper in this case. Between JP

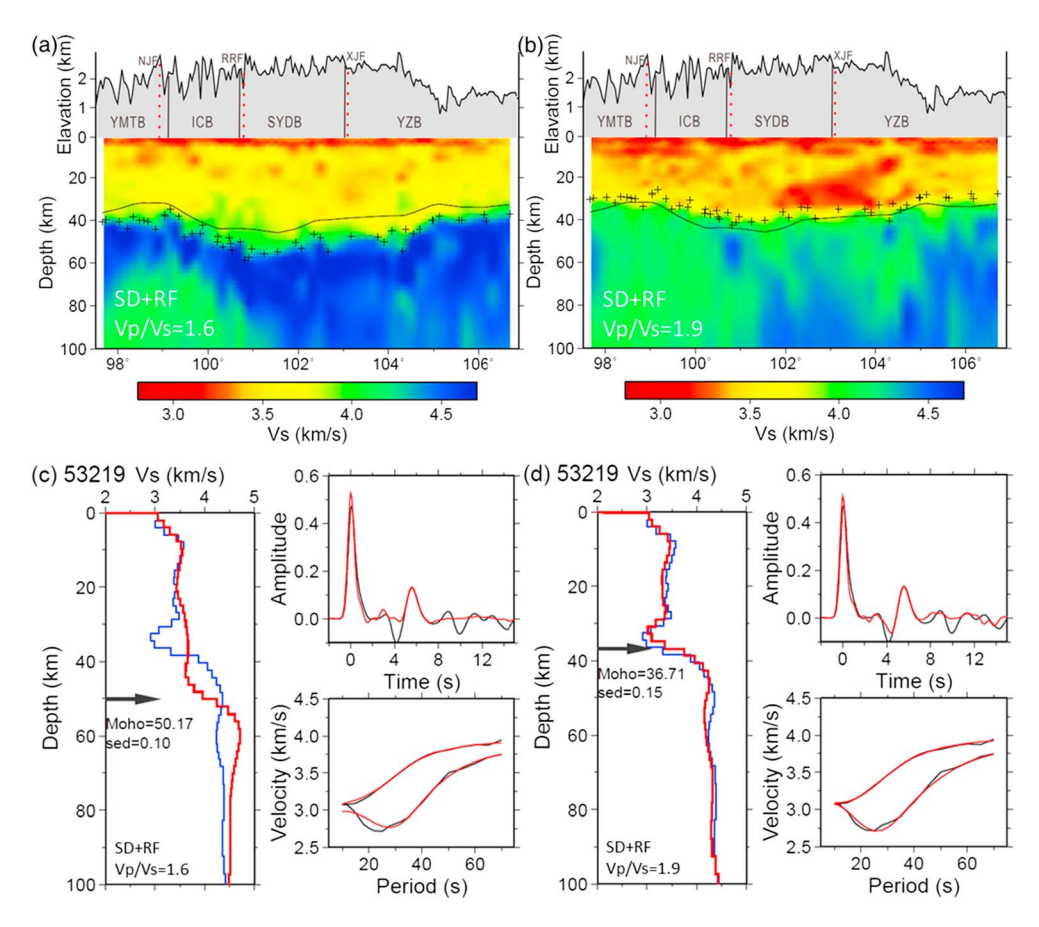


Figure 10. *S* velocity profiles and examples on station 53219 from joint inversions of RF and dispersions (with sedimentary layer) using fixed extreme V_p/V_s ratios of (a and c) 1.6 and (b and d) 1.9. In Figures 10a and 10b, topography and geological elements are shown at the top. The black crosses mark the Moho from joint inversions, and the black line shows the same smoothed Moho as in Figure 6 from the JP. In Figures 10c and 10d, the inversion results and synthetics are in red and the observed RFs and dispersion curves are in black. The inversion results are compared with that from the JP (blue) in Figure 7c. As a reference, the average crustal V_p/V_s at station 53219 from the JP is 1.853.

and SD + RF, LVZ1 is stronger and the shape stands out better in JP, and the LVZ2 also shows up better in JP. Furthermore, the low-velocity structures in the mantle below LVZ1 and LV2 are more coherent and clearer in JP than in any other images.

To test further the influence of an unknown V_p/V_s ratio, we conducted joint inversions with dispersions and RF only using the lower and upper bounds of the V_p/V_s ratio (1.6 and 1.9, respectively) for this profile (Figures 10a and 10b). The differences are clear both in the crust and in the mantle. The prominent LVZ1 even disappears completely if we use $V_p/V_s = 1.6$ (Figure 10a). The data fits for the extreme V_p/V_s values at example station 53219 (Figures 10c and 10d) (with an average crustal V_p/V_s of 1.853 from the JP) are indistinguishable compared with the joint inversion results (Figures 7a and 7c), except that with $V_p/V_s = 1.6$ the negative amplitude before Ps was not well recovered. The tests demonstrate once again the trade-offs of model parameters, and if the V_p/V_s value has a large departure, the model differences are not only on the Moho but also on the velocity structures in both the crust and the mantle (Figures 10a and 10c).

4.1.3. Moho and Crustal V_p/V_s Ratio

It is well known that the Moho depth (H) trades off with V_p/V_s ratio (k) in the inversion of the RF of the Ps converted wave (e.g., Zhu & Kanamori, 2000). Essentially,

$$t_{PS} = \frac{H}{V_S} \left(\sqrt{1^2 - p^2 V_S^2} - \sqrt{k^{-2} - p^2 V_S^2} \right)$$
 (2)

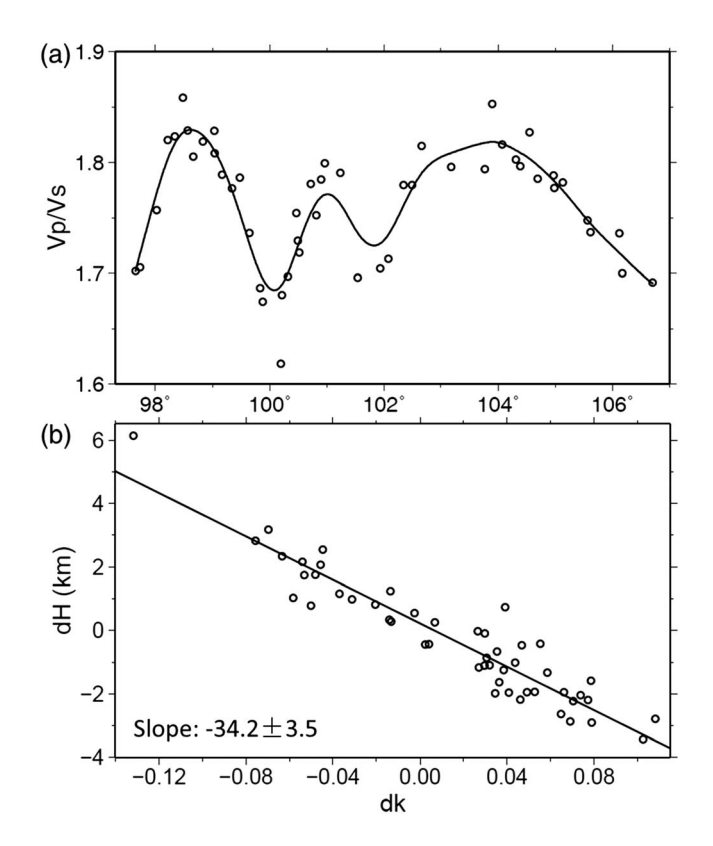


Figure 11. Summary of the inversion results on V_p/V_s ratio (k) and Moho depth (H) from the JP. (a) The average crustal V_p/V_s ratios along the profile with a spline fit. The averaged ratio is calculated from the V_p/V_s profile of the JP. (b) Plot of the Moho variation (dH, relative to SD + RF in Figure 9c) versus the variation of the averaged crustal V_p/V_s (dk = k - 1.75) from the JP. The black line is the result of the linear regression.

where t_{Ps} is the time separation between Ps and direct P and p is the ray parameter of the incident wave. The average V_s in the crust can be constrained by the dispersion curves. Given the average crustal V_s , the Moho depth depends strongly on the crustal V_p/V_s ratio to fit the same Ps arrival in the RF. The larger V_p/V_s ratio would result in shallower Moho. This is clear in the comparisons of the tomographic images (Figures 9 and 10). Between JP and SD + RF (Figures 9a and 9c), the Moho shifts are up to \sim 6.1 km and the standard deviation of the shifts is \sim 1.9 km.

Figure 11a summarizes the V_p/V_s ratio averaged over the whole crust for each station. The averaged values range from about 1.62 to 1.86. Figure 11b summarizes the departure of the average crustal V_p/V_s ratio and Moho depth in JP (with Vp) from SD + RF (assuming $V_p/V_s = 1.75$). The dH/dk slope is -34.2 ± 3.5 km/1, which amounts to 6.8 km if k changes by 0.2, which is similar to what we expect from equation (2) (e.g., Zhu & Kanamori, 2000).

4.2. Comparison With a Previous Study

We now compare the results from the JP and from the previous study by SUN14, which used dispersion and RF data only. SUN14 also used H-k method of receiver functions (Zhu & Kanamori, 2000) to estimate the V_p/V_s ratio. They used a linearized inversion of dispersion and RF for the layered V_s structure. The layered parameterization at shallow depth can account for the effect of the sedimentary layer to some extent, and SUN14 indeed shows some very slow velocities at surface. However, because of the variable thickness and elastic property of the sedimentary layer, a layered structure is not effective in accounting for the contribution of the layer to the RF waveform. Indeed, compared to SD + RF (Figure 9c), the S velocity image in SUN14 (their Figure 4) is more similar to SD + RF-sed, including low-velocity anomalies in the

upper crust, the deeper LVZ1 and the shallower LVZ2, and the high-velocity layer above the Moho, all of which are indications of not accounting properly for the sedimentary layer as discussed above.

In summary, we confirm that the JP results are generally consistent with SUN14, including the presence of LVZ1 and LVZ2. However, comparing the two is very similar to comparing the JP and SD + RF-sed. Thus, relative to SUN14, significant differences from the JP include the following: (1) the shallow upper crust structure, as the result of the inclusion of the sedimentary layer; (2) the strength and depth range of the LVZs (clearer in JP; LVZ1 becomes deeper at 20–40 km compared to 15–30 km in SUN14, while LVZ2 becomes shallower above 14 km compared to 10–20 km in SUN14); (3) the Moho depth below the two crustal LVZs becomes shallower due to higher V_{ρ}/V_{s} ratios; and (4) more coherent and clearer low-velocity structures in the mantle between the two crustal LVZs.

The V_p/V_s ratios derived from RFs only by SUN14 shows large scatter. While the values are relatively stable at 1.6 to 1.8 for the YZB (east of 103°E or so), the values scatter from 1.6 to 2.0 west of it. The large scatter reflects the uncertainty of the H-k method when the quality of the later multiple converted phases of the RF is poor. On the other hand, the averaged crustal V_p/V_s values from the JP show systematic variations (Figure 11a). Large average V_p/V_s values are located in the vicinities of the major crustal block boundaries, beneath NJF, RRF, and XJF.

Undoubtedly, the results from the JP are influenced by the uncertainties in the fixed P wave model. We have examined several P models and chose a favorite one for this study (see section 3.1). However, if we choose any of the models, we expect an improvement from the JP over SD + RF with fixed $V_p/V_s = 1.75$. Furthermore, our basic conclusions of this study (on crustal LVZs and V_p/V_s ratios, and mantle structures) would remain the same. A clue is to look at the comparison between JP and SD + RF (Figures 9a and 9c),

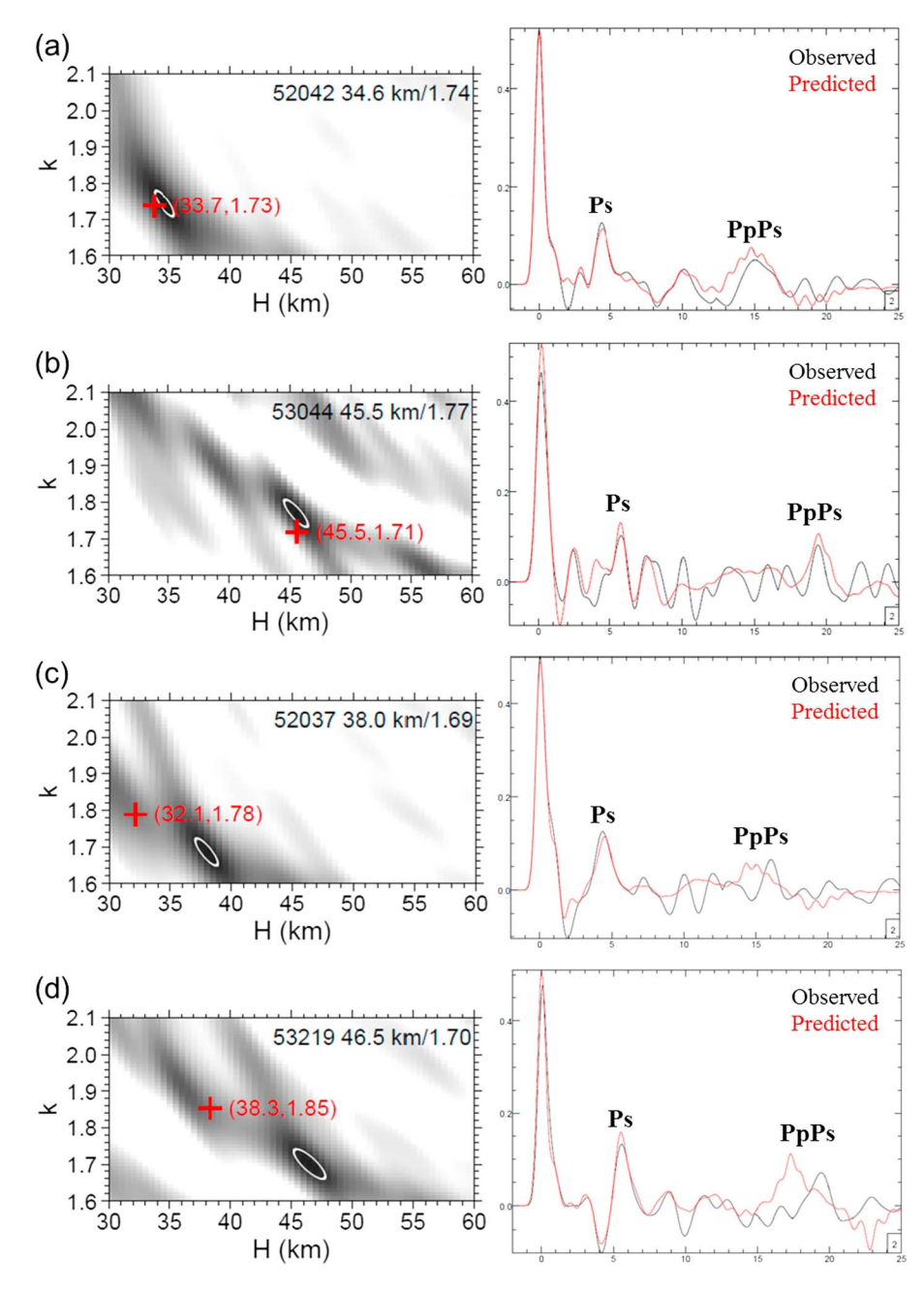


Figure 12. Examples of stations where (a and b) the joint inversion results agree with H-k and can predict the time of PpPs phase and (c and d) they do not agree. The red crosses mark the results of Moho depth and crustal V_p/V_s from JP. The black and red traces are the observed RFs (the Ps and PpPs phases have been corrected by moveouts with distances) and the predicted RFs calculated using the obtained velocity models from JP, respectively.

which is discussed above. The images are quite similar, although the JP image is sharper and more coherent and clearer. Basically, if the V_p/V_s differs by less than 0.05, the difference between inversions is not large (Figure 10d). The synthetic test in Figure 2a also shows the tolerance of the P model inaccuracy in the JP—The V_p at a location may not be accurate, but if the average V_p is correct, it still helps in the JP. Another clue is the systematic variations in the V_p/V_s ratios from the JP (Figures 6f and 11a), which correlate with crustal blocks and are hardly random. Thus, we argue that a reasonable (but less perfect) P velocity model can provide a better constraint on the joint inversion of dispersions and RFs than simply assuming a fixed V_p/V_s .

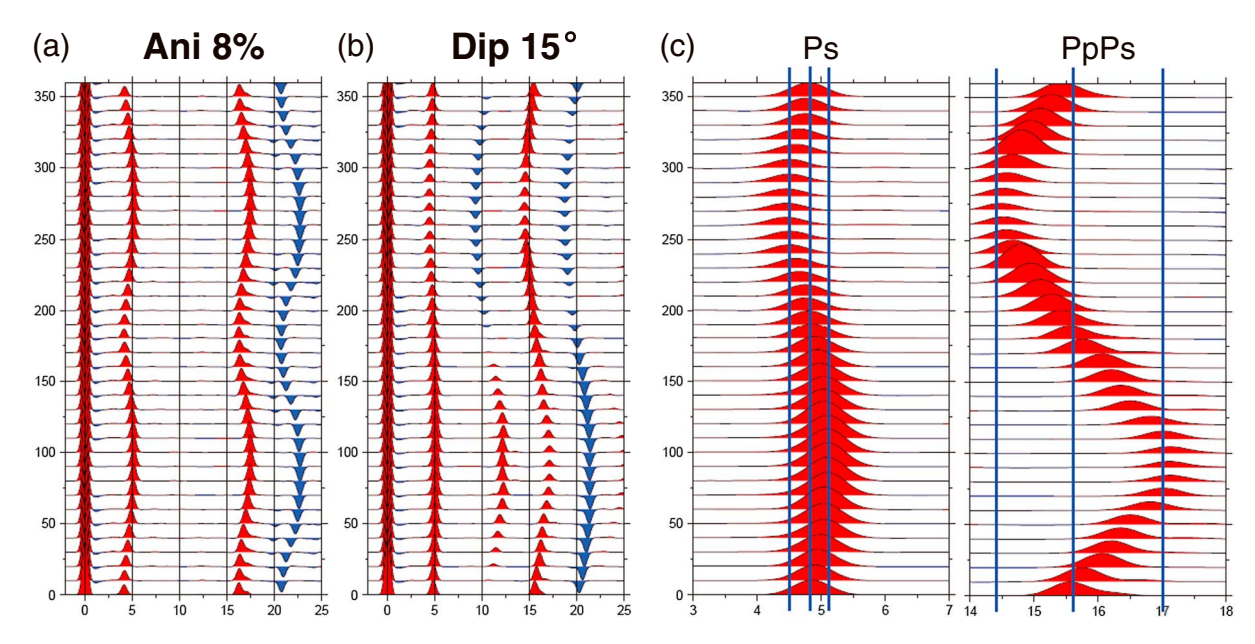


Figure 13. Synthetic RFs along azimuth (vertical axes) for (a) 8% crustal anisotropy, (b) 15° Moho dipping, and (c) 15° Moho dipping of enlarged view, relative to a two-layer model with a 40-km crust. The blue lines in Figure 13c mark the offsets of *Ps* and *PpPs* due to dipping Moho.

The LVZ1 structure in the mid-lower crust can be readily explained by partial melt as proposed by SUN14. Its correlation with very high V_p/V_s ratio (greater than 1.9 or Poisson's ratio greater than 0.31) from our new imaging provides strong additional support (Christensen, 1996; Owens & Zandt, 1997). However, different from the interpretation in SUN14, the JP results suggest that the LVZ2 structure may not be due to crustal melting at all. In SUN14, the LVZ2 was at 10–20 km depth in the middle crust. However, the JP with the inclusion of by a sedimentary layer indicates that the LVZ2 is limited to the upper crust (shallower than ~14 km), which does not fall in the depth range of mid-lower crustal flow. The depth range is well within the brittle part of the upper crust, and many active faults exist in the area with strong topographic variation. A low-velocity anomaly can also be seen down to ~10 km depth beneath a surface valley at ~105.2°E in the YZB. On the other hand, the V_p/V_s ratios in LVZ2 are not as high as in LVZ1. Thus, we interpret LVZ2 as the indication of active major fault zones at the upper crust depth instead of partial melt. Furthermore, slightly high V_p/V_s ratios are observed beneath major crustal block boundaries NJF and RRF throughout the crust without significant LVZs (Figure 6f).

Bai et al. (2010) reported two zones of low electric resistivity at similar locations, one at depth of 20–40 to 100 km at LVZ1 location and the other at 20 to 70 km at LVZ2 location. The LVZ1 low resistivity may be explained by low-velocity partial melting crust and uppermost mantle. However, the LVZ2 low resistivity is unlikely related to the shallow upper crust low velocities because of the depth difference and the high rigidity of the shallow upper crust; rather, the low resistivity anomaly is likely related to the uppermost mantle low velocities, the elevated Moho, and the relatively high V_p/V_s throughout the crust.

4.3. Comparison Between JP and H-k Results: Issues About Crustal Multiples

Multiple converted phases can help resolving the ambiguity in the well-known *H-k* method (Zhu & Kanamori, 2000). But they are usually much more difficult to identify than the *Ps* phase, which was an important motivation for the current study. Here we compared results from the *H-k* method and the JP.

We examined the H-k stackings for all the stations in this study. The majority (some 80%) of H-k plots do not show strong energy of crustal multiples. For the stations that have relatively stronger and clearer energy (with smaller error ellipses in the H-k plots), we found some stations where the joint inversion results agree with H-k but many other stations where the two methods disagree. A couple of examples for each case are shown in Figure 12. The disagreements can be clearly observed between the predicted multiples (PpPs phase, in particular) for the JP and the multiples in the observed RFs.

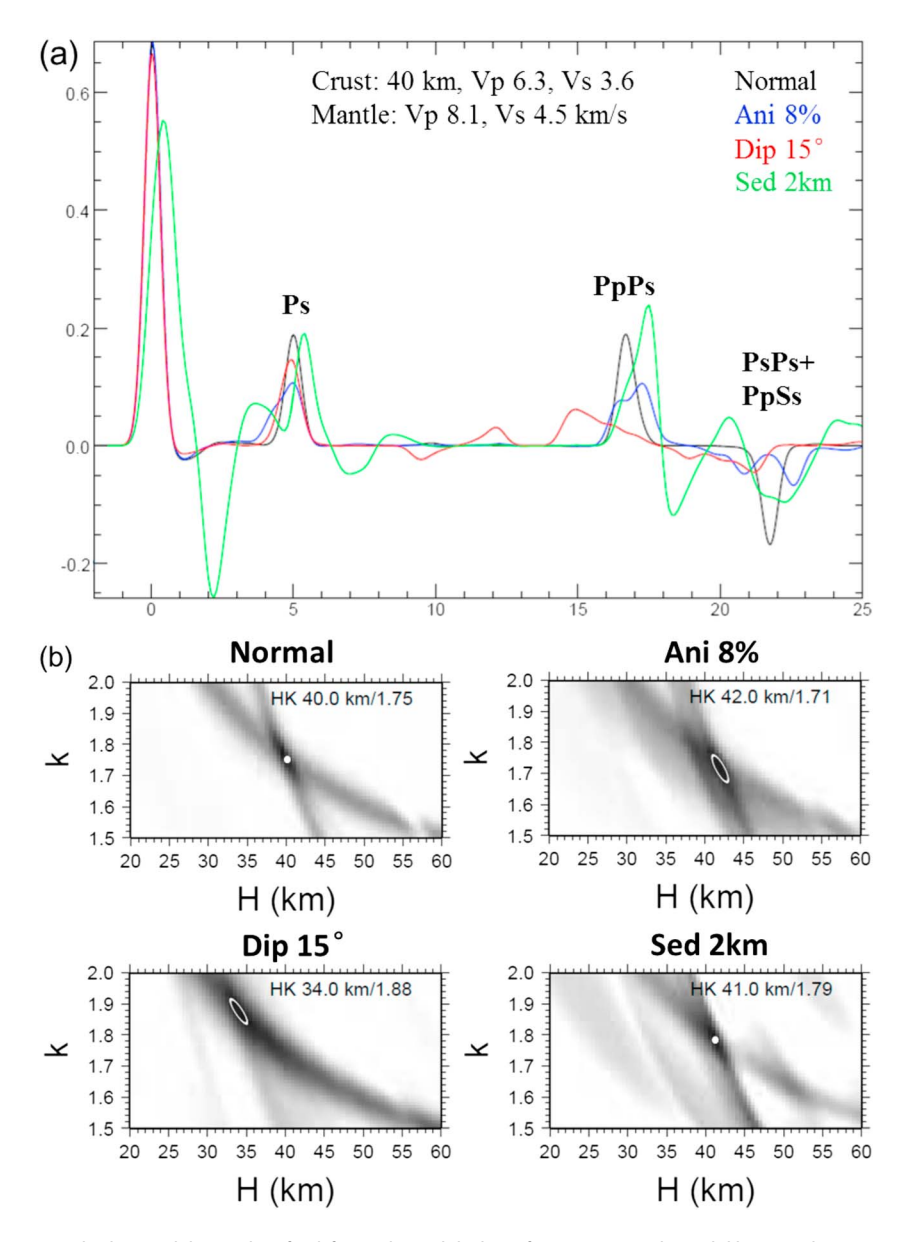


Figure 14. (a) Stacked RF and (b) results of H-k for each model. The reference (normal) model has a 40 km crust with crustal V_p of 6.3 km/s and V_s of 3.6 km/s ($V_p/V_s = 1.75$), and with mantle V_p of 8.1 km/s and V_s of 4.5 km/s ($V_p/V_s = 1.8$). The black, blue, red, and green lines in Figure 14a are calculated for the normal model, with 8% crustal anisotropy, with 15° Moho dipping, and with a 2 km sedimentary layer, respectively. The normal and Sed-2 km cases in Figure 14b have very small error; thus, the result is shown by a white dot.

The crustal structure in SE Tibet is complex, which has significant crustal anisotropy and Moho dipping (Bao et al., 2015a; Sun et al., 2014; Xu & Song, 2010). The crustal complexity can influence the multiples of the RFs more than the *Ps* phase. To understand the discrepancy between the JP and the *H-k* results, we performed several synthetic tests with more complex model than a 1-D isotropic model. Crustal anisotropy and dipping Moho would generate azimuthal variation in the traveltime of the *Ps* phase as well as in the traveltimes of the multiples. Using the Raysum code by Frederiksen and Bostock (2000), we found that the effect of azimuthal anisotropy on multiples is almost the same as on *Ps*, while the effect of a dipping Moho on multiples is about 5 times of that on *Ps* (Figure 13). The relation nearly remains the same when the anisotropy strength or the Moho dip changes. The Gaussian width and ray parameter used in the synthetics are 2.5 and 0.06 s/km, respectively.

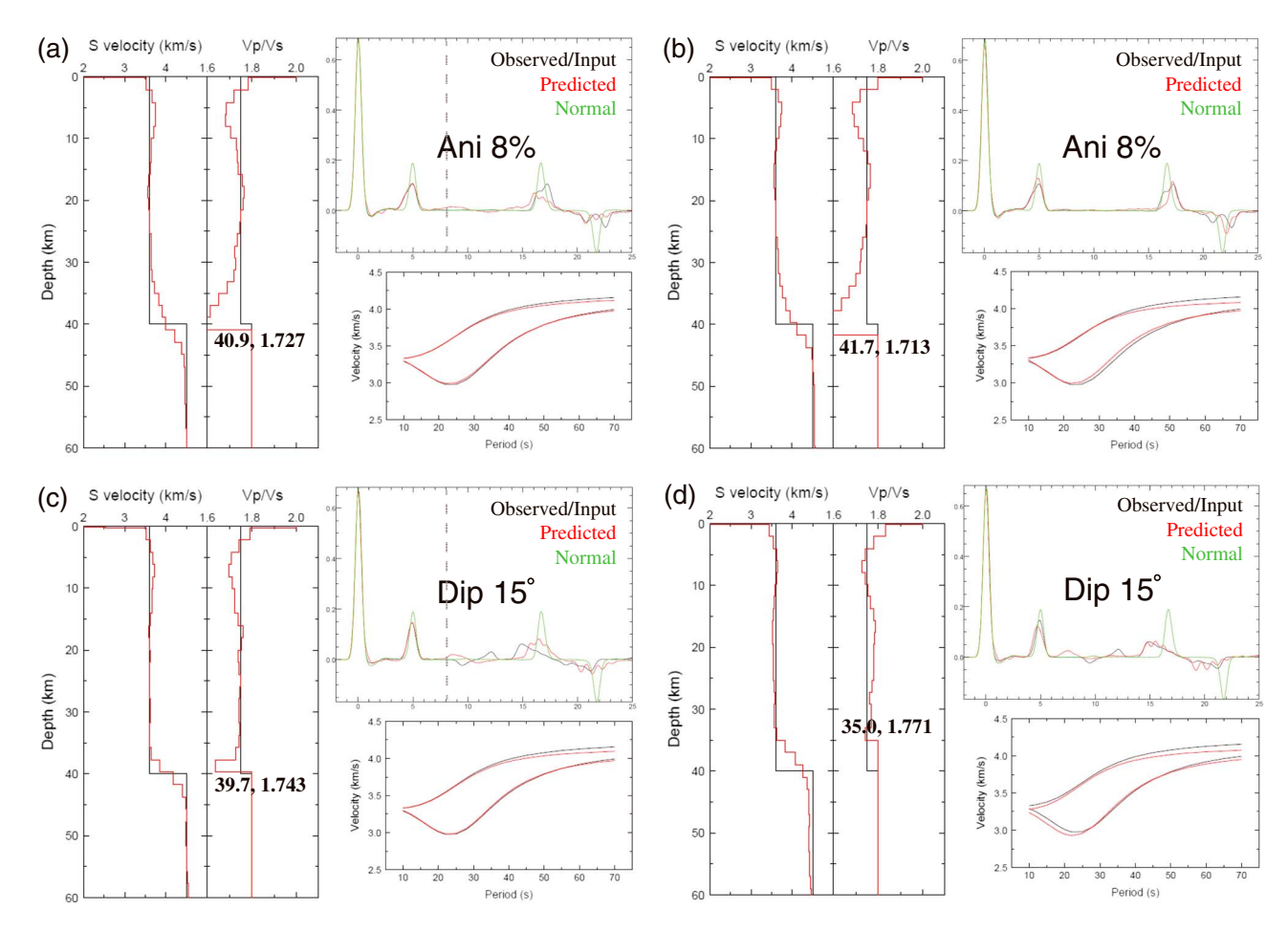


Figure 15. Results of JP for (a and b) model with 8% crustal anisotropy and (c and d) model with 15° Moho dipping. Figures 15a and 15c used only the RF before the grey dashed line (-2 to 8 s) to exclude the multiples, while Figures 15b and 15d used -2 to 25 s to include the multiples in the JP. The part after 8 s in Figures 15a and 15c is predicted from the final model of JP. In all the panels, the black lines show the observed or input and the red lines show the predicted. The green trace is the RF from the normal 40 km crust model (Figure 14; $V_p/V_s = 1.75$, without anisotropy or Moho dip) as a reference. The numbers in the V_p/V_s panels are the Moho depth and average crustal V_p/V_s from JP.

We performed H-k stacking and joint inversion (JP) with synthetic RFs (Figures 14a). We considered four models for the H-k (Figure 14): (1) a normal case with one-layer crust as reference, (2) with 8% crustal anisotropy, (3) with 15° Moho dipping, and (4) with a 2 km sedimentary layer. In the stacked RFs (Figure 14a), we see significant changes in waveforms, traveltimes, and amplitudes, relative to the normal case. The changes in the multiples are much greater than in the Ps, particularly for the dipping Moho case. For comparison, we performed JP for cases 2 and 3, either without multiples or with RF multiples (Figure 15) (we can reproduce the input models using the JP for the normal and sedimentary-layer cases using the Ps only as we have showed extensively above). Crustal anisotropy would blur the H-k plot (Figure 14b) and make the Moho transition gradual in JP and change the V_p/V_s depth profile significantly (Figures 15a and 15b). The anisotropy causes azimuthal variation of the traveltimes of Ps and multiples (Figure 13) so that the stacked trace shows reduced amplitudes and distorted waveforms (Figure 14a). Thus, the gradual Moho (and consequently significantly reduced V_p/V_s at the bottom of the crust) is needed to fit the RF as best as possible. Still whether the multiples are included (Figure 15b) or not (Figure 15a), the models are quite similar and both can fit the Ps reasonably well but neither can fit the multiples perfectly. The dipping Moho has the greatest effect on the waveform of the multiples (time and amplitude) among the cases we considered (Figure 14a). If we include the multiples, both the JP (Figure 15d) and the H-k (Figure 14b) have large errors with a similar Moho offset of ~6 km and a V_p/V_s offset of 0.13 in H-k. While the JP inversion without the multiples (Figure 15c) cannot fit the multiples, the recovery is acceptable. The tests demonstrate that it is better not



to use the multiples in the JP when the crust is not simple, as the H-k method or JP including the multiples can result in large errors.

In the SE Tibet, the Moho dipping and crustal anisotropy have been found to be guite strong with large azimuthal variation of Ps RFs (e.g., Bao et al., 2015a; Sun et al., 2014; Xu & Song, 2010). On the other hand, the nonuniform azimuthal coverage of RFs would also certainly bias the stacked RF. Furthermore, the combination of anisotropy, Moho dipping, sedimentary layer, and intracrustal interfaces would make the later arriving multiples complicated. Even when the multiples are strong and the H-k stack is very robust (with small error ellipse), the result can be wrong if the crustal structure is not simple (Figure 14). We are working on systematic corrections to the multiples to improve the H-k stacking. Before that, the multiples should not be included in the joint inversions, and we urge caution in interpreting H-k results when there is a reason to believe the crust is complex.

5. Conclusions

We present a joint inversion scheme that incorporates surface-wave dispersions, receiver functions, and the P velocity profile. The model is parameterized using a sedimentary layer at the surface and two connecting splines for the crust and mantle, respectively. The thickness of the sedimentary layer and the depth of the Moho are allowed to change. The crustal spline has a uniform node spacing, while the node spacing of the mantle spline increases with depth. We used the NA to search for the model parameters with parallel computing. We applied the method to a dense linear array in SE Tibet, previously studied by SUN14. Extensive tests using synthetic and real data suggest that the method is suitable and robust for a variety of velocity structures and Moho discontinuities and provides constraints on crustal V_D/V_S profiles. The flexibility of the parameterization and the inclusion of the V_p constraint are crucial in the improved model recovery. The inclusion of a sedimentary layer is also important to fit the beginning part of RFs; an inversion without it may result in artifacts in both shallow and deep crust. Comparison of joint inversions with and without V_D model shows general agreement for the array profile. However, significant differences are clearly observable, including the shape and depth of LVZs, Moho depth, and mantle structure. The addition of a reasonable (even when it is less perfect) V_p model is more desirable than simply assuming a fixed V_p/V_s in such a joint inversion. Complex crustal structures (anisotropy, Moho dipping, sedimentary layer, and possible intracrustal interfaces) have much stronger influence on the RF multiples (on both amplitudes and traveltimes) than on the Ps phase. Under such cases, the results from the H-k method can be wrong even when the multiples are strong. We suggest that systematic corrections on the crustal multiples are needed before they can be used in joint inversion or a modified H-k method.

The results from the new joint inversion show two LVZs observed by SUN14. Prominent LVZ1 located in the mid-lower crust under the Xiaojiang fault area correlates with anomalously high V_D/V_s ratios, suggesting possible partial melting. However, the other LVZ (LVZ2) was imaged in the brittle shallow upper crust (down to depth of ~14 km), which is likely associated with crustal fault zones rather than partial melting as previously claimed. The major boundaries between crustal blocks show relatively high V_p/V_s ratios throughout the crust. We observed clear low-velocity structure in the mantle beneath the two crustal LVZs with elevated Moho, which may suggest mantle upwelling and the influence of mantle processes on crustal deformation.

Acknowledgments

The original seismic data of the station array were from ChinArray-Himalaya (2011). We thank the careful and constructive reviews from two anonymous reviewers, which helped improve the manuscript. Most figures were prepared using Generic Mapping Tools (GMT) (Wessel & Smith, 1998). The study was supported by the National Science Foundation (EAR 1620595), National Natural Science Foundation of China (41774056), and Department of Geology, University of Illinois at Urbana-Champaign.

References

Agius, M. R., & Lebedev, S. (2014). Shear-velocity structure, radial anisotropy and dynamics of the Tibetan crust. Geophysical Journal International, 199, 1395-1415.

Ammon, C. J., Randall, G. E., & Zandt, G. (1990). On the nonuniqueness of receiver function inversions. Journal of Geophysical Research: Solid Earth, 95, 15,303-15,318. https://doi.org/10.1029/JB095iB10p15303

Bai, D., Unsworth, M. J., Meju, M. A., Ma, X., Teng, J., Kong, X., ... Liu, M. (2010). Crustal deformation of the eastern Tibetan plateau revealed by magnetotelluric imaging. Nature Geoscience, 3(5), 358-362.

Bao, X., Sun, X., Xu, M., Eaton, D. W., Song, X., Wang, L., ... Wang, P. (2015a). Two crustal low-velocity channels beneath SE Tibet revealed by joint inversion of Rayleigh wave dispersion and receiver functions. Earth and Planetary Science Letters, 415, 16–24.

Bao, X., Song, X., & Li, J. (2015b). High-resolution lithospheric structure beneath Mainland China from ambient noise and earthquake surface-wave tomography, Earth and Planetary Science Letters, 417, 132-141,

Chen, H., Zhu, L., & Su, Y. (2016). Low velocity crustal flow and crust-mantle coupling mechanism in Yunnan, SE Tibet, revealed by 3D S-wave velocity and azimuthal anisotropy. Tectonophysics, 685, 8-20.



- ChinArray-Himalaya (2011). China Seismic Array waveform data of Himalaya Project, Institute of Geophysics, China Earthquake Administration, https://doi.org/10.12001/ChinArray.Data, Himalaya
- Christensen, N. I. (1996). Poisson's ratio and crustal seismology. Journal of Geophysical Research: Solid Earth, 101, 3139–3156. https://doi.org/ 10.1029/95JB03446
- Clark, M. K., & Royden, L. H. (2000). Topographic ooze: Building the eastern margin of Tibet by lower crustal flow. Geology, 28(8),
- Deng, Y., Shen, W., Xu, T., & Ritzwoller, M. H. (2015). Crustal layering in northeastern Tibet: A case study based on joint inversion of receiver functions and surface wave dispersion. Geophysical Journal International, 203, 692-706.
- Ding, Z., & Wu, Z. (2013). Advances of ChinArray program, paper presented at 2013 AGU Fall Meeting, AGU, San Francisco, CA.
- Dong, H., Wei, W., Jin, S., Ye, G., Zhang, L., Jing, J., ... Jones, A. G. (2016). Extensional extrusion: Insights into south-eastward expansion of Tibetan Plateau from magnetotelluric array data. Earth and Planetary Science Letters, 454, 78-85.
- England, P., & Houseman, G. (1986). Finite strain calculations of continental deformation 2. Comparison with the India-Asia collision zone. Journal of Geophysical Research: Solid Earth, 91, 3664-3676. https://doi.org/10.1029/JB091iB03p03664
- Frederiksen, A. W., & Bostock, M. G. (2000). Modelling teleseismic waves in dipping anisotropic structures. Geophysical Journal International, 141.401-412.
- Hearn, T. M. (1996). Anisotropy Pn tomography in the west United States. Journal of Geophysical Research, 101, 8403-8414. https://doi.org/ 10.1029/96JB00114
- Hearn, T. M., Wang, S., Pei, S., Xu, Z., Ni, J., & Yu, Y. (2008). Seismic amplitude tomography for crustal attenuation beneath China. Geophysical Journal International, 174(1), 223-234.
- Herrmann, R. B. (2013). Computer programs in seismology: An evolving tool for instruction and research. Seismological Research Letters, 84,
- Huang, J., Zhao, D., & Zheng, S. (2002). Lithospheric structure and its relationship to seismic and volcanic activity in southwest China. Journal of Geophysical Research: Solid Earth, 107(B10), 2255. https://doi.org/10.1029/2000JB000137
- Huang, R., Wang, Z., Pei, S., & Wang, Y. (2009). Crustal ductile flow and its contribution to tectonic stress in Southwest China. Tectonophysics,
- Huang, Z., Wang, P., Xu, M., Wang, L., Ding, Z., Wu, Y., ... Li, H. (2015). Mantle structure and dynamics beneath SE Tibet revealed by new seismic images. Earth and Planetary Science Letters, 411, 100-111.
- Julià, J., Ammon, C. J., Herrmann, R. B., & Correig, A. M. (2000). Joint inversion of receiver function and surface wave dispersion observations. Geophysical Journal International, 143(1), 99-112.
- Kennett, B. L. N., & Engdahl, E. R. (1991). Travel times for global earthquake location and phase identification. Geophysical Journal International, 105, 429-465.
- Langston, C. A. (1979). Structure under Mount Rainier, Washington, inferred from teleseismic body waves. Journal of Geophysical Research: Solid Earth, 84, 4749-4762. https://doi.org/10.1029/JB084iB09p04749
- Le Pape, F., Jones, A. G., Vozar, J., & Wei, W. (2012). Penetration of crustal melt beyond the Kunlun Fault into northern Tibet. Nature Geoscience,
- Lei, J., Zhao, D., & Su, Y. (2009). Insight into the origin of the Tengchong intraplate volcano and seismotectonics in southwest China from local and teleseismic data. Journal of Geophysical Research: Solid Earth, 114, B05302. https://doi.org/10.1029/2008JB005881
- Li, M., Zhang, S., Wang, F., Wu, T., & Qin, W. (2016). Crustal and upper-mantle structure of the southeastern Tibetan Plateau from joint analysis of surface wave dispersion and receiver functions. Journal of Asian Earth Sciences, 117, 52-63.
- Li, Y., Pan, J., Wu, Q., & Ding, Z. (2014). Crustal and uppermost mantle structure of SE Tibetan plateau from Rayleigh-wave group velocity measurements. Earthquake Science, 27(4), 411–419.
- Liang, C., & Song, X. (2006). A low velocity belt beneath northern and eastern Tibetan Plateau from Pn tomography. Geophysical Research Letters, 33, L22306. https://doi.org/10.1029/2006GL027926
- Liang, C., Song, X., & Huang, J. (2004). Tomographic inversion of Pn travel times in China. Journal of Geophysical Research: Solid Earth, 109, B11304. https://doi.org/10.1029/2003JB002789
- Molnar, P., & Tapponnier, P. (1975). Cenozoic tectonics of Asia—Effects of a continental collision. Science, 189(4201), 419-426.
- Nafe, J. E., & Drake, C. L. (1963). Physical properties of marine sediments. In M. N. Hill (Ed.), The Sea (Vol. 3, pp. 794-815). New York:
- Owens, T. J., & Zandt, G. (1997). Implications of crustal property variations for models of Tibetan plateau evolution. Nature, 387, 37-43.
- Ozalaybey, S., Savage, M. K., Sheehan, A. F., Louie, J. N., & Brune, J. N. (1997). Shear-wave velocity structure in north basin and range province from the combined analysis of receiver functions and surface waves. Bulletin of the Seismological Society of America, 87, 183–189.
- Royden, L. H., Burchfiel, B. C., King, R. W., Wang, E., Chen, Z., Shen, F., & Liu, Y. (1997). Surface deformation and lower crustal flow in eastern Tibet, Science, 276(5313), 788-790.
- Royden, L. H., Burchfiel, B. C., & van der Hilst, R. D. (2008). The geological evolution of the Tibetan Plateau. Science, 321(5892), 1054–1058. Sambridge, M. (1999). Geophysical inversion with a neighbourhood algorithm—I. Searching a parameter space. Geophysical Journal International, 138, 479-494
- Shapiro, N. M., & Ritzwoller, M. H. (2002). Monte-Carlo inversion for a global shear velocity model of the crust and upper mantle. Geophysical Journal International, 151, 88-105.
- Shen, W., Ritzwoller, M. H., Schulte-Pelkum, V., & Lin, F.-C. (2013). Joint inversion of surface wave dispersion and receiver functions: A Bayesian Monte-Carlo approach. Geophysical Journal International, 192(2), 807-836.
- Sun, X., Bao, X., Xu, M., Eaton, D. W., Song, X., Wang, L., ... Li, H. (2014). Crustal structure beneath SE Tibet from joint analysis of receiver functions and Rayleigh wave dispersion. Geophysical Research Letters, 41, 1479-1484. https://doi.org/10.1002/2014GL059269
- Sun, X. L., Song, X., Zheng, S., Yang, Y., & Ritzwoller, M. H. (2010). Three dimensional shear wave velocity structure of the crust and upper mantle beneath China from ambient noise surface wave tomography. Earthquake Science, 23, 449-463.
- Tapponnier, P., Xu, Z., Roger, F., Meyer, B., Arnaud, N., Wittlinger, G., & Yang, J. (2001). Oblique stepwise rise and growth of the Tibet Plateau. Science, 294, 1671-1677.
- Wang, C., Chan, W., & Mooney, W. D. (2003). Three-dimensional velocity structure of crust and upper mantle in southwestern China and its tectonic implications. Journal of Geophysical Research, 108(B9), 2442. https://doi.org/10.1029/2002JB001973
- Wei, W., Sun, R., & Shi, Y. (2010). P-wave tomographic images beneath southeastern Tibet: Investigating the mechanism of the 2008 Wenchuan earthquake. Science in China Series D: Earth Sciences, 53, 1252-1259.
- Wessel, P., & Smith, W. H. F. (1998). New, improved version of generic mapping tools released. Eos, Transactions American Geophysical Union, 79(47), 579-579.



- Xu, Z., & Song, X. (2010). Joint inversion for crustal and Pn velocities and Moho depth in Eastern Margin of the Tibetan Plateau. *Tectonophysics*. 491, 185–193.
- Xu, Z., Song, X., & Zhu, L. (2013). Crustal and uppermost mantle S velocity structure under Hi-CLIMB seismic array in central Tibetan Plateau from joint inversion of surface wave dispersion and receiver function data. *Tectonophysics*, 584, 209–220.
- Yang, Y., Ritzwoller, M. H., Zheng, Y., Shen, W., Levshin, A. L., & Xie, Z. (2012). A synoptic view of the distribution and connectivity of the mid-crustal low velocity zone beneath Tibet. *Journal of Geophysical Research: Solid Earth, 117*, B04303. https://doi.org/10.1029/2011JB008810
- Yao, H. J., Beghein, C., & van der Hilst, R. D. (2008). Surface wave array tomography in SE Tibet from ambient seismic noise and two-station analysis—II. Crustal and upper-mantle structure. *Geophysical Journal International*, 173, 205–219.
- Yin, A., & Harrison, T. M. (2000). Geologic evolution of the Himalayan-Tibetan orogen. *Annual Review of Earth and Planetary Sciences*, 28, 211–280.
- Yuan, X., Ni, J., Kind, R., Mechie, J., & Sandvol, E. (1997). Lithospheric and upper mantle structure of southern Tibet from a seismological passive source experiment. *Journal of Geophysical Research: Solid Earth, 102, 27,*491–27,500. https://doi.org/10.1029/97JB02379
- Zhang, P., Shen, Z., Wang, M., Gan, W., Burgmann, R., Monlar, P., ... You, X. (2004). Continuous deformation of the Tibetan Plateau from global positioning system data. *Geology*, 32, 809–812.
- Zhao, D., Hasegawa, A., & Horiuchi, S. (1992). Tomographic imaging of P and S wave velocity structure beneath northeastern Japan. *Journal of Geophysical Research: Solid Earth, 97*, 19,909–19,928. https://doi.org/10.1029/92JB00603
- Zhao, L., Xie, X., He, J., Tian, X., & Yao, Z. (2013). Crustal flow pattern beneath the Tibetan Plateau constrained by regional Lg-wave Q tomography. *Earth and Planetary Science Letters*, 383, 113–122.
- Zheng, C., Ding, Z., & Song, X. (2016). Joint inversion of surface wave dispersion and receiver functions for crustal and uppermost mantle structure in Southeast Tibetan Plateau. *Acta Geophysica Sinica*, *59*(9), 3223–3236.
- Zhu, L., & Kanamori, H. (2000). Moho depth variation in southern California from teleseismic receiver functions. *Journal of Geophysical Research: Solid Earth, 105*, 2969–2980. https://doi.org/10.1029/1999JB900322